KeAi
CHINESE ROOTS
GLOBAL IMPACT

Available online at www.keaipublishing.com/en/journals/journal-of-magnesium-and-alloys/

ScienceDirect

Journal of Magnesium and Alloys 20 (2026) 102109

www.elsevier.com/locate/jma

Full Length Article

Identifying Fe-bearing inclusions in electrolytic magnesium and deep purification via Ti-Si trapping

Bingbing Gao, Bo Yang, Rui Zheng, Boyu Liu*, An Wang, Jiuzhang Li, Hangwei Cui, Zhiwei Shan*

State Key Laboratory for Mechanical Behavior of Materials, Engineering Research Center for Magnesium-based New Materials, Center for Advancing Materials Performance from the Nanoscale (CAMP-Nano), Xi'an Jiaotong University, Xi'an 710049, PR China

Received 14 February 2026; received in revised form 30 March 2026; accepted 20 April 2026
Available online 15 May 2026

Abstract

Electrolytic primary magnesium generally contains elevated Fe impurities, which severely degrade corrosion resistance, thus limiting downstream use. Although vacuum sublimation, in principle, should separate Fe from magnesium because Fe is far less volatile, the purified condensate frequently remains Fe-rich. Here we identify that Fe resides mainly in micrometer-scale inclusions (elemental Fe and Fe-bearing intermetallic particles). Through analysis of the drag force exerted by magnesium vapor on these inclusions, we determine that they can be entrained in the vapor stream, thus bypassing separation based solely on volatility difference. To intercept these particles, we implement an in-line filtration positioned in an appropriate thermal zone along the vapor route, and select Ti mesh packed with Si particles as the interception medium based on thermal stability, affinity for impurity species, and cost. In controlled comparisons using industrial electrolytic magnesium (258 ppm Fe), sublimation alone lowers Fe to 76 ppm, Ti-mesh filtration lowers it to 28 ppm, and Ti-Si integrated trapping to 4 ppm, meeting the Mg9999 specification without detectable Ti or Si contamination. These results establish particulate entrainment as a principal barrier to deep purification by sublimation and provide a practical framework for upgrading electrolytic magnesium via targeted particle interception and rational trap design.

© 2026 Chongqing University. Publishing services provided by Elsevier B.V. on behalf of KeAi Communications Co. Ltd.
This is an open access article under the CC BY-NC-ND license (http://creativecommons.org/licenses/by-nc-nd/4.0/)

Keywords: Electrolytic magnesium; Purification; Vacuum sublimation; Fe-bearing impurities; Particle entrainment.

1. Introduction

Magnesium and its alloys have low density, high specific strength, good damping capacity, and excellent biocompatibility, making them attractive for aerospace, transportation, electronics, and biomedicine applications [1–3]. Primary magnesium is the essential raw material for producing downstream alloy products, and its quality directly affects the alloy performance [4–6]. Industrial production of primary magnesium mainly relies on two methods: Pidgeon process, a silicothermic reduction of calcined dolomite, and electrolytic process [7], in which brine is dehydrated to anhydrous $MgCl_2$ and then electrolyzed to metallic magnesium. In the following texts, we term the primary magnesium produced by electrolytic process as electrolytic magnesium for simplicity. In addition, methods such as vacuum carbothermal reduction and electrolysis of magnesium oxide (MgO) for producing primary magnesium have also been actively investigated [8,9]. Currently, Pidgeon process is the dominant method for producing primary magnesium, but it remains batch-wise and less automated [10,11]. In contrast, the electrolysis method offers continuous, highly automated operation [12,13]. However, a drawback of electrolytic magnesium is its elevated Fe and Ni content, introduced by HCl used for brine dehydration. The acid corrodes storage tanks and pipelines, dissolving Fe (and Ni) that are carried into the $MgCl_2$ feedstock and ultimately into the magnesium melt [14,15].

Elevated Fe severely degrades the corrosion resistance of magnesium and its alloys. Classic work reported that magne-

Peer review under the responsibility of Chongqing University
* Corresponding authors.
E-mail addresses: boyuliu@xjtu.edu.cn (B. Liu), zwshan@xjtu.edu.cn (Z. Shan).

https://doi.org/10.1016/j.jma.2026.102109
2213-9567/© 2026 Chongqing University. Publishing services provided by Elsevier B.V. on behalf of KeAi Communications Co. Ltd. This is an open access article under the CC BY-NC-ND license (http://creativecommons.org/licenses/by-nc-nd/4.0/)

sium has good corrosion resistance but becomes highly susceptible once impurity levels exceed tolerance thresholds [16]. The reported Fe tolerance in magnesium is ~170 ppm [17], but it falls further in the presence of Si or Al, which interact with Fe to form cathodic intermetallic compounds that drive galvanic corrosion [18–20]. For example, with Si present, increasing Fe merely from 3 ppm to 25 ppm raised the corrosion rate of magnesium in 3.5% NaCl from 0.22 mm/y to 106.67 mm/y, nearly a 500-fold jump [21]. Ni exhibits an even lower tolerance threshold (5 ppm) than Fe [16], due to the formation of Mg_2Ni phases with high cathodic activity [22]. This extreme sensitivity to Fe and Ni has constrained the usage of electrolytic magnesium and underscores the necessity for its additional purification. Notably, although electrolytic magnesium contains higher levels of Fe and Ni than Pidgeon magnesium [23], other impurities (such as Al, Mn, Si, and Zn) are markedly lower, already meeting or closely approaching the 4N Mg standard (Fig. 1). Consequently, if Fe and Ni are removed without introducing secondary contamination, electrolytic magnesium can achieve 4N purity, enabling high-end applications like reductants for electronic grade titanium, degradable biomedical devices, and high-performance alloys that demand low impurity levels.

A commonly used method for removing Fe from magnesium is flux refinement [24]. Additives such as Ti and $ZrCl_4$ are used as flux agents that react with Fe to form insoluble intermetallic compounds (Fe_2Ti, $FeZr_3$) that settle from the magnesium melt during static settling [25,26]. This method can reduce Fe content to above 20 ppm [27–30], which meets the 3N5A standard but does not reach the 4N standard. Moreover, the excessive use of flux agents will in turn introduce impurities. The maximum solubility of Ni in magnesium reaches 40 ppm at the eutectic temperature (780 K), far exceeding the 5 ppm corrosion tolerance threshold [31], making the removal of Ni from magnesium melt only by settling very difficult.

Vacuum distillation can effectively remove the impurities by exploiting differences in melting/sublimation points and saturated vapor pressures [32,33]. When heated to near the melting point of magnesium (~ 923 K), magnesium evaporates readily, whereas Fe and Ni with much higher melting points (~ 1723 K) and lower saturated vapor pressures (~ 10^{-11} Pa) remain in the residue, enabling effective separation. Vacuum distillation can reduce Fe and Ni to <10 ppm [34–39]. The trade-off is throughput and cost: to suppress co-evaporation of high-melting-point impurities like Fe and Ni, vacuum distillation is typically conducted near the melting point of magnesium, which however slows evaporation rate [40]. In addition, the distillation system often employs multi-stage condensation baffles arranged along the decreasing temperature gradient. Only baffles located at optimal temperatures can collect high-purity magnesium. Baffles set at high temperatures collect magnesium co-condensed with less-volatile and high-melting-point impurities (Fe, Si, etc.), while baffles set at low temperatures capture magnesium enriched in more-volatile and low-melting-point impurities (K, Na, and Zn, etc.). This leads to the low yields of high-purity product. Revel [41] reported a yield of high-purity magnesium (≥4N) below 40% during vacuum distillation at 973 K. As a result, a multi-cycle distillation is often required.

To overcome these difficulties, a purification mechanism based on selectively separating impurities from magnesium in gaseous state has been proposed [42]. Magnesium and impurities are first quickly heated into the vapor phase at elevated temperatures to ensure a high evaporation rate. The magnesium and impurities flow passes through a controlled temperature gradient (stepwise cooling) where magnesium and impurities condense according to their distinct saturated vapor pressures, removing most impurities having different saturated vapor pressures and condensation temperatures with magnesium. For impurities with condensation behavior similar to magnesium, an adsorption/filtration device that can react with impurities without capturing Mg is set in the gas flow route. This combined approach accelerates separation while maintaining efficiency, and has successfully produced 99.99% magnesium in just a single operation directly by the Pidgeon method [42].

The present work validated the efficiency of this method in purifying electrolytic magnesium. The difficulty is that the impurity profile of electrolytic magnesium differs markedly from Pidgeon magnesium: Fe and Ni are much higher. We therefore identified the forms of Fe and Ni present, designed targeted removal pathways, and selected adsorption/filtration media accordingly. The results showed that the contents of Fe and Ni were reduced to 4 ppm and 1 ppm, respectively, achieving a high-purity magnesium of 99.995%.

2. Experimental methods

The primary magnesium ingots used in this study were produced via electrolysis by Qinghai Salt Lake Magnesium Industry Co., Ltd.. The impurity concentrations in the raw and purified magnesium were determined by Inductively Coupled Plasma Mass Spectrometry (Agilent 7800 ICP-MS). Samples were dissolved in nitric acid and hydrochloric acid. The instrument was calibrated using multi-element standard solutions at six concentration levels, and the calibration curves exhibited correlation coefficients (R^2) greater than 0.999 for all target elements. The limit of quantification for both Fe and Ni in the solid samples is 1 ppm. To ensure data accuracy, each sample was measured in duplicate following the standard procedure, and the relative standard deviations (RSD) for all reported values were <5%.

This study employed a six-zone temperature-controlled tube furnace, which consists of heating, vacuum, water-cooling, and reaction systems. Silicon carbide heaters can achieve 1773 K with independent zone control, establishing an axial temperature gradient. The corundum furnace tube features a threaded high-purity graphite liner sealed by stainless steel flanges. A rotary vane pump maintains <10 Pa vacuum, while a chiller recirculates coolant through flange ports to prevent thermal overload. Electrolytic magnesium ingots were loaded into graphite crucibles and assembled within the corundum furnace tube. The experiments were conducted at

1073 K under a vacuum of <10 Pa. In this study, three sets of purification experiments were performed: vacuum sublimation without any filter material, sublimation with a titanium mesh, and sublimation with a titanium mesh packed with silicon particles. The titanium mesh and silicon particles used in the experiments were purchased, both with a purity of 99.9%. The titanium mesh had a wire diameter of 90–100 μm and an aperture size of 140–150 μm, while the silicon particles ranged from 5 to 10 mm in size. The titanium mesh was cut into a circular piece approximately 4 cm in diameter and placed between two sections of the graphite tube. An eight-hole graphite plate with a hole diameter of 6 mm was positioned beneath the mesh to secure it, and silicon particles were then tightly packed onto the mesh to form the Ti-Si filter. The high-purity magnesium crystallized at the condensation end was collected and analyzed by ICP-MS. The sublimation residues and captured particulates on the filters were characterized by scanning electron microscopy (SEM), energy-dispersive spectroscopy (EDS), and X-ray diffraction (XRD).

3. Results and discussion

3.1. The content, morphology, composition, and forms of Fe and Ni impurities in electrolytic magnesium

3.1.1. Elevated Fe and Ni in electrolytic magnesium

The typical impurity content in industrial electrolytic crude magnesium is shown in Fig. 1 [38,43]. The Fe content in electrolytic magnesium varies between batches, typically ranging from 100 to 350 ppm, far above the 30 ppm requirement of 3N5A Mg standard (GB/T 3499–2023). The Ni content fluctuates from 5 to 20 ppm. In the electrolytic magnesium used in this work, the average Fe and Ni contents are 280.4 ppm and 12.3 ppm, respectively, both exceeding the 3N5A Mg standard. In contrast, other impurities like Al, Mn, Si, Zn, Sn, Pb, and Cu in electrolytic magnesium are much lower, which already meet or closely approach the 4N Mg standard (GB/T 3499–2023). An important advantage of electrolytic magnesium is its low Zn content, notable because Zn is among the

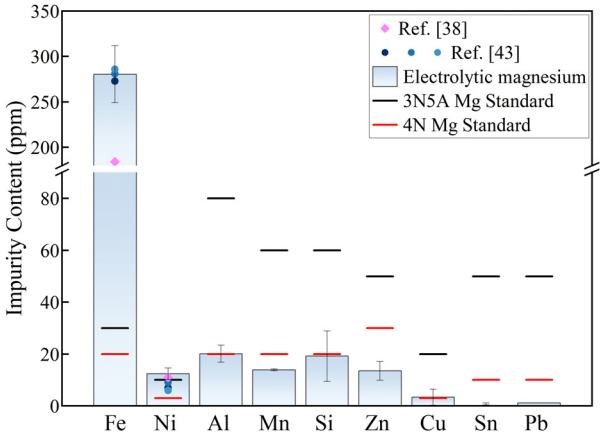


Fig. 1. Impurity contents in industrial magnesium ingots prepared by electrolytic process, which have high Fe content and low content of Al, Mn, Si, Zn, Sn, Pb, and Cu impurities.

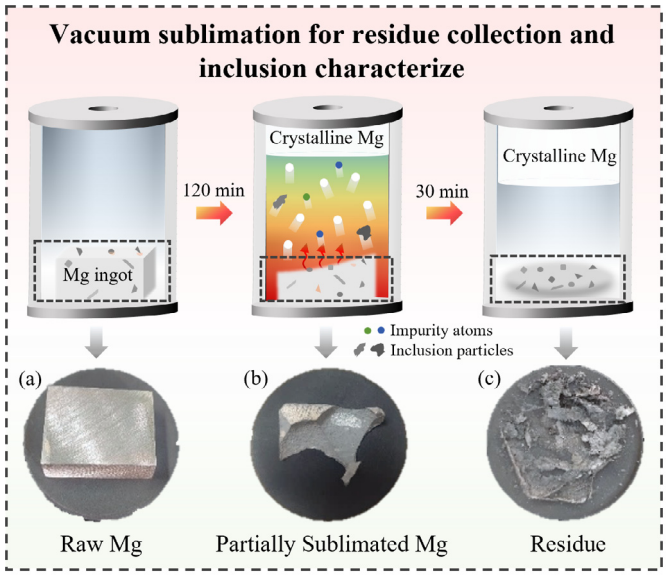


Fig. 2. Vacuum sublimation at 923 K to characterize the impurities in electrolytic magnesium. (a) The sample was cut from as-received electrolytic magnesium. (b) Partially sublimed magnesium with inclusions exposed on the evaporated surface. (c) Residue enriched in non-volatiles after complete sublimation.

most difficult impurities to remove due to its saturated vapor pressure and melting/sublimation characteristics being close to those of magnesium. Consequently, the effective reduction of Fe and Ni without introducing new impurities would enable the production of 4N-purity magnesium from this electrolytic feedstock. These observations motivate our focus on targeted removal of Fe and Ni in the following sections.

3.1.2. Morphology and composition of Fe, Ni-bearing inclusions in electrolytic magnesium

Since the content of Fe far exceeds its solubility in electrolytic magnesium, Fe-bearing inclusions, including elemental Fe particles or Fe-containing compounds, are expected in the magnesium ingots. To determine their composition and forms, vacuum sublimation experiments at 923 K (near the melting point of magnesium) were employed (Fig. 2). Under these conditions, magnesium evaporates readily owing to its high saturated vapor pressure, whereas Fe and its compounds, both with much higher melting points and far lower vapor pressures, are expected to remain essentially non-volatile and concentrate in the residue. Operating at a relatively low temperature limits the entrainment of impurities into vapor and preserves the inclusions for analysis.

Two fractions are collected: partially sublimed magnesium and the post-sublimation residue. The partially sublimed surface is irregular and concave (Fig. 3a). Higher-magnification images reveal numerous particles with bright contrast in a uniform distribution across the evaporated surface (Fig. 3b). EDS identified two predominant particle types: cubic Fe-rich particles and blocky Ni-rich particles. The cubic particles are primarily composed of Fe, with minor Al and Si. This compositional profile suggests that Al and Si are either dissolved

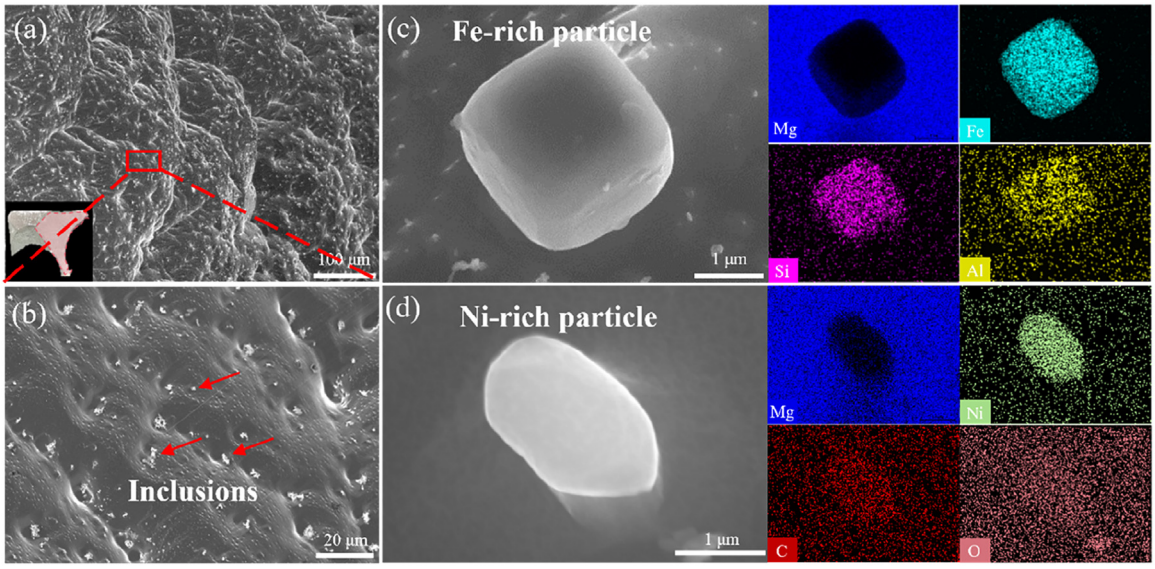


Fig. 3. Fe-rich and Ni-rich inclusions on evaporated surfaces. (a) SEM image of the side surface of a partly sublimed magnesium; (b) Magnified view from (a) showing the particles; (c–d) SEM-EDS of representative individual Fe-Al-Si and Mg-Ni particles.

in the Fe matrix or have formed intermetallic compounds that encapsulate primary Fe particles. The blocky particles are rich in Mg and Ni, suggesting the coexistence of Mg and Ni. Considering that Mg and Ni can form intermetallics [22], some of Ni impurities in the electrolytic magnesium would be in the form of Mg-Ni intermetallics (Fig. 3d). In addition, we also carefully searched and characterized the inclusions with Fe and Ni in the original electrolytic magnesium (as shown in Supplementary Fig. 1). Their compositions are generally consistent with the observations and characterizations described above by EDS mapping.

To confirm impurity phases, we analyzed the residue after complete sublimation by XRD. Fig. 4a shows the collected residue. We first performed SEM-EDS mapping to quickly examine the particles, which revealed two dominant features: granular particles enriched in Fe, Al, and Si, in line with the individual particle level observations in Fig. 3, and flocculent regions rich in Mg and O, indicating magnesium oxide. For clarity, Fe-rich particles and MgO are pseudocolored yellow and cyan, respectively. XRD identified elemental Fe, Al_3FeSi_2, $Fe_{0.42}Si_{2.67}$, and MgO (Fig. 4b). The particles are predominantly <10 μm, with a mean size of 2.3 μm. Ni-bearing phases are not detected by XRD but are only sporadically detected in the residue, consistent with their much lower bulk abundance relative to Fe. Notably, these Fe-rich phases are nearly absent in sublimation residues from low-Fe magnesium (magnesium ingot obtained by silicothermic reduction and distillation), indicating that they are attributed to the high-Fe content in the electrolytic magnesium feedstock.

3.1.3. Forms of Fe-bearing impurities

The measured Fe in the studied electrolytic magnesium sample (258 ppm) far exceeds its equilibrium solubility ($\sim$ 10 ppm at the eutectic and even lower at room temperature). Most Fe must therefore reside in undissolved phases. Consistent with XRD, Fe occurs as elemental particles and as Fe-Al-Si and Fe-Si intermetallics (Al_3FeSi_2 and $Fe_{0.42}Si_{2.67}$), with only a minor fraction in solid solution.

Using the measured content of Al (23.9 ppm) and Si (24.3 ppm), we estimate the Fe tied up in intermetallics. Assuming all Al enters Al_3FeSi_2, the required Si is 2/3 of the Al content, leaving the remainder of Si to form $Fe_{0.42}Si_{2.67}$. Converting ppm to moles per kg and applying these stoichiometries gives:

$$\text{Fe in } Al_3FeSi_2:\ n(Fe) = n(Al)/3 = \sim 16.5 \text{ ppm Fe}$$

$$\text{Fe in } Fe_{0.42}Si_{2.67}:\ n(Fe) = 0.42/2.67(\text{Si leftover}) = \sim 2.4 \text{ ppm Fe}$$

Thus, if all Al and Si form these intermetallic phases, they account for only about 18.9 ppm Fe. Adding $\sim$ 10 ppm Fe in solid solution leaves $\sim$ 229.1 ppm Fe unaccounted for, which we attribute to elemental Fe particles. It should be noted that this calculated 18.9 ppm Fe in intermetallics represents an upper-bound estimate, as some Al can be dissolved in the magnesium matrix. Consequently, the actual Fe content in intermetallics is likely lower, and the proportion of elemental Fe particles is correspondingly higher than estimated. The data are summarized in Table 1.

3.2. Strategies for Fe- and Ni-bearing impurities removal

3.2.1. The general principle

Guided by the identified impurity forms and their thermodynamic properties (Table 1), we designed a three-stage purification process involving evaporation, gradient condensation, and selective adsorption/filtration. First, the electrolytic magnesium ingot is evaporated at 1073 K to generate a magnesium vapor flux while retaining non-volatile impurities and

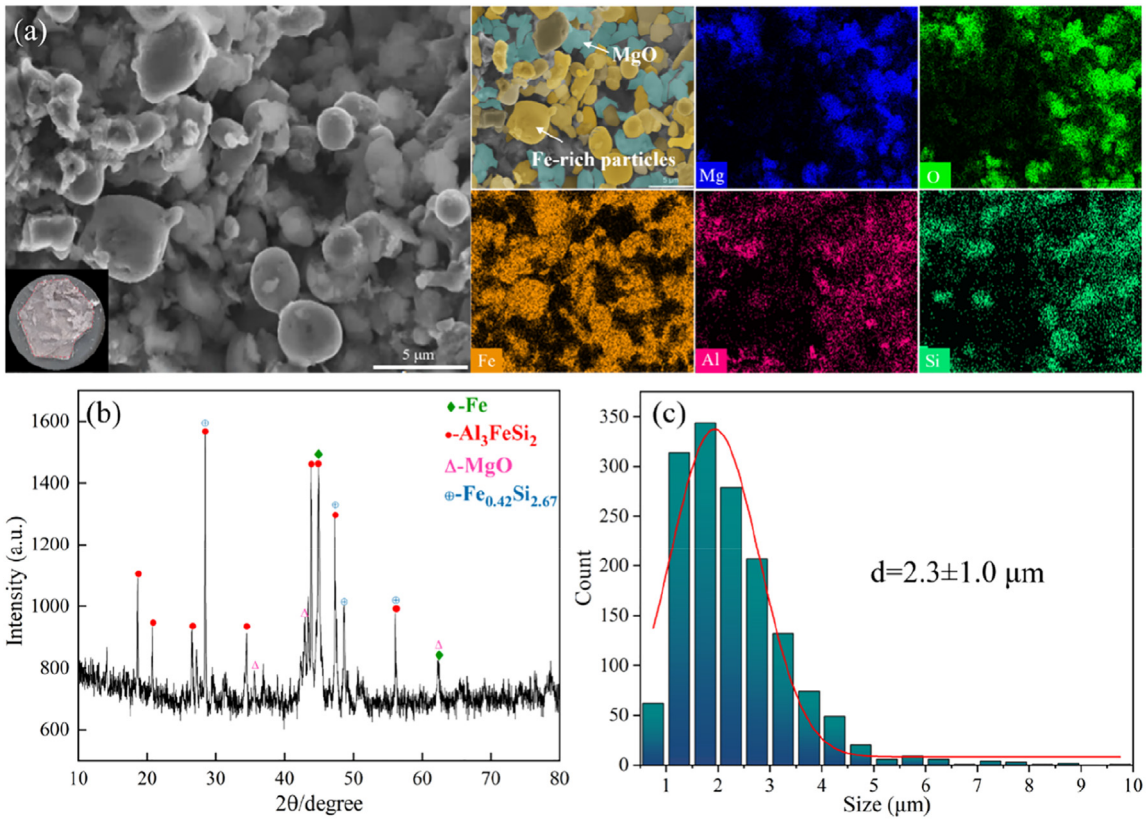


Fig. 4. Phase constitution and size distribution of residue particles. (a) SEM images with EDS distinguishing Fe-rich and MgO (pseudocoloured yellow and cyan); (b) XRD identifying elemental Fe, Al_3FeSi_2, $Fe_{0.42}Si_{2.67}$, and MgO phases; (c) Particle-size distribution.

Table 1
Estimated forms, contents and proposed removal strategies for Fe impurities in electrolytic magnesium.

Forms of Fe impurities		Estimated Contents (ppm)	Removal Mechanism
Solid solution of Fe in Mg matrix		~10	• Low-temperature sublimation to leave Fe concentrated in the residue • Chemical adsorption by specific filter materials
Intermetallics	Al_3FeSi_2	~16.5	• Low-temperature sublimation to leave particles in the residue
	$Fe_{0.42}Si_{2.67}$	~2.4	• Physical interception by filter materials and inertial collision.
Elemental Fe		~229.1	

inclusions in the residue as far as possible. Second, a controlled temperature gradient forces Fe, Ni, and the compounds to condense before magnesium, achieving an initial separation. Third, the vapor passes through a filter that preferentially binds Fe and Ni and intercepts the Fe-, Ni-bearing compounds and magnesium oxides, while with minimal interaction with magnesium. Finally, purified magnesium vapor is crystallized in a low-temperature condenser.

To set operating windows and predict performance, we (1) computed saturated vapor pressures of Fe and Ni versus temperature and estimated theoretical separation limit of sublimation; (2) calculated transport of entrained particulates (Fe, MgO, and Fe-bearing compounds) in the magnesium vapor flow; and (3) screened filter media by melting point offsets relative to magnesium, formation energies with Mg/Fe/Ni, and cost, leading to a final selection that was validated experimentally.

3.2.2. Thermodynamic analysis of Fe and Ni elements during vacuum sublimation

During sublimation, the volatility of Fe and Ni relative to magnesium is governed by their saturated vapor pressures P* (T), expressed as [44]:

$$\log P^*(Pa) = A/T + B\log T + CT + D \quad (2.1)$$

where T is in kelvin, and A-D are element-specific evaporation constants (tabulated in Ref. [45]) and used below to compute P* for Mg, Fe, and Ni. Impurities with a higher P* are

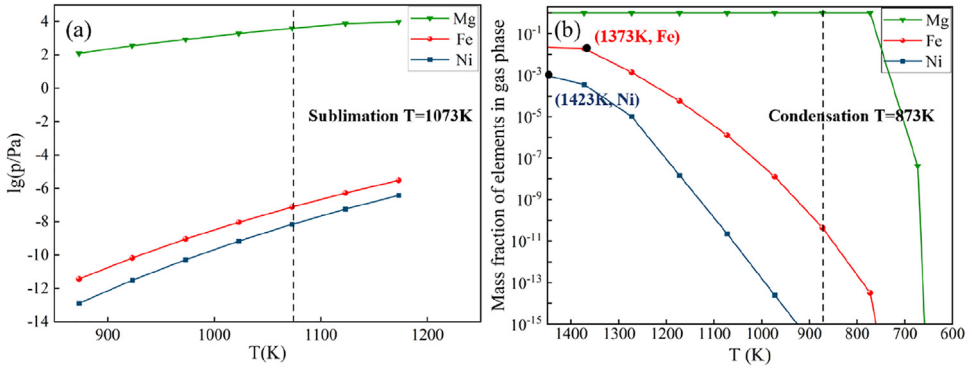


Fig. 5. The estimated sublimation and condensation behavior of magnesium, Fe, and Ni. (a) Saturated vapor pressure of Fe, Ni, and Mg with temperature from equation 2.1. (b) Gas-phase mass fractions of Fe, Ni, and Mg during cooling.

more volatile. At the chosen evaporation temperature 1073 K, the P* of Fe and Ni are 11 and 12 orders of magnitude lower than Mg, respectively (Fig. 5a), which suggests a negligible co-sublimation of Fe and Ni with magnesium. Moreover, thermodynamic calculations (Fig. 5b) indicate that Fe and Ni start condensing at temperatures substantially higher than that of magnesium (~1373 K and ~1423 K, respectively). Even assuming complete volatilization, the residual gaseous concentrations of Fe and Ni fall below 10^{-12} upon cooling to the actual condensation temperature of 823 K, demonstrating that both impurities almost completely condensed before the arrival of the Mg vapor at the condenser. Thus, an appropriate sublimation-condensation window can in principle efficiently separate Fe and Ni from magnesium.

However, the sublimation analysis above assumes thermodynamic equilibrium and thus likely overestimates the separation effect. In practice, non-equilibrium transport can carry more Fe and Ni into the magnesium vapor than predicted. Moreover, elemental Fe particles and Fe-bearing intermetallic particles (Al_3FeSi_2 and $Fe_{0.42}Si_{2.67}$) can be entrained by magnesium vapor stream then incorporated into the condensed magnesium, bypassing volatility-based separation. These realities motivate the downstream selective adsorption/filtration process detailed next.

3.2.3. Movement of impurity particles during vacuum sublimation

In a rarefied Mg vapor stream, an entrained particle experiences three dominant forces: the gravitational force (G_P), the buoyancy force (F_B), and the fluid drag force (F_R) [46]. Effects from added mass, Basset, Magnus, and Saffman lift are negligible under our conditions [47], and with particles initially at rest on the Mg surface, inertial terms can be omitted. The force balance is illustrated in Fig. 6.

For a particle of diameter d_p, projected area A_p and volume V_p in the F_R, F_B, and G_P are calculated by the following equations,

$$F_R = \frac{1}{2}\rho_g v_g^2 A_p C_D \tag{3.1}$$

$$F_B = \rho_g g V_p \tag{3.2}$$

$$G_P = \rho_p g V_p \tag{3.3}$$

where ρ_g and v_g are the density (kg/m^3) and flow velocity (m/s) of magnesium vapor; ρ_p, A_p, V_p and d_p are the density (kg/m^3), area (m^2), volume (m^3) and diameter (m) of impurity particles, respectively, C_D is the resistance coefficient, g is the gravitational acceleration (9.81 m/s^2).

If an impurity particle were blown upward by the magnesium gas flow, the sum of the F_R and F_B should be greater than G_P, that is

$$F_R + F_B - G_P \geq 0 \tag{3.4}$$

$$\rho_p \leq \rho_g \left(1 + \frac{3C_D v_g^2}{4 d_p\, g}\right) \tag{3.5}$$

Equation (3.5) defines the critical particle density (ρ_p) versus particle size (d_p) that can be entrained by magnesium vapor. To determine ρ_p and d_p, the magnesium vapor velocity (v_g) and resistance coefficient (C_D) should be known. The v_g can be calculated by

$$v_g = \frac{\omega}{\rho_g} \tag{3.6}$$

$$\omega = \frac{m_0 - m_t}{\Delta t \times A} \tag{3.7}$$

$$\rho_g = \frac{P M_g}{RT} = \frac{0.02431 P}{8.314 T} = 0.00292 \frac{P}{T} \tag{3.8}$$

where ω is the actual evaporation rate (kg/(m^2·s)), m_0 and m_t are the initial and final magnesium masses (kg), Δt is the sublimation time (s), A is the surface area of the magnesium (m^2), ρ_g is the density of magnesium vapor (kg/m^3), M_g is the molar mass of Mg (0.02431 kg/mol), R is the universal gas constant (8.314 J/(mol·K)). P is the saturated vapor pressure of magnesium (Pa), and T is the temperature (K).

The resistance coefficient C_D depends on the magnesium vapor flow regime. The Reynolds number classifies flow into three classes: laminar flow, transitional flow, and turbulent

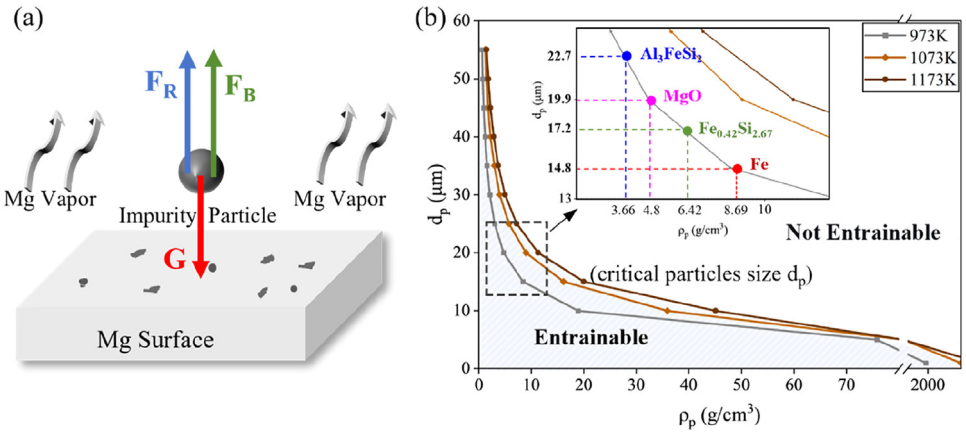


Fig. 6. Analysis of inclusion particles that can be entrained by the magnesium vapor flow. (a) Force diagram of an impurity particle within magnesium vapor flow. (b) Relationship between critical density and size of impurity particles that can be entrained by magnesium vapor at various temperatures.

flow [48]. The particle Reynolds number (*Re*) is given by [49]:

$$Re = \frac{\rho_g v_g d_p}{\eta_g} \tag{3.9}$$

where η_g is the viscosity of magnesium vapor (Pa·s), which is calculated by the following equation [49],

$$\eta_g = \frac{\rho_g \bar{v}_g \lambda_g}{3} = \frac{1}{3} \cdot \frac{PM_g}{RT} \cdot 1.6\sqrt{\frac{RT}{M_g}} \cdot \frac{kT}{\sqrt{2}\pi d^2 P}$$
$$= 8.748 \times 10^{-7} \cdot \sqrt{T} \tag{3.10}$$

By calculating ρ_g, v_g, and η_g and substituting them into equation (3.9), we can determine that in the temperature range of 973 K to 1173 K and for particle sizes between 1 μm and 100 μm, the Reynolds number (*Re*) is much lower than 1, confirming Stokes laminar flow. Thus, the resistance coefficient follows C_D=24/Re_p.

Substituting C_D into Eq. (3.5) yields the critical density-size relationship for particle entrainment in Mg vapor, plotted as a set of curves at variant temperatures in Fig. 6b. Inclusion particles whose density and size fall below the curve are susceptible to being entrained by the magnesium flow with the given parameters. For the dominant inclusions (Fe, Al_3FeSi_2, $Fe_{0.42}Si_{2.67}$, and MgO) in electrolytic magnesium, the critical particle sizes for entrainment all exceed 10 μm. The experimentally measured size distribution (Fig. 4c) shows that the vast majority of particles are below 10 μm. Therefore, a significant fraction of inclusions can be entrained under the present sublimation conditions, necessitating the placement of a filter within the vapor transport channel to achieve effective interception.

3.3. Filter material selection

During sublimation, filter materials can physically intercept and chemically react with impurities to remove them. The filter materials should satisfy the following criteria: (1) High melting points that ensure the filter materials are stable and do not melt or sublimate during work under high temperatures. (2) Do not react with Mg to avoid contamination. (3) High affinity for impurity elements. (4) Safety, non-toxicity, and more importantly, cost-efficiency. Initial screening based on the melting point criterion (1) identified Si, Mn, Ti, Cr, Cu, Zr, W, Co, and Sc. The formation energy between specific elements indicates the tendency of the interaction between them. More negative values indicate greater thermodynamic stability of intermetallic compounds, reflecting a stronger binding tendency. As shown in Table 2 and Fig. 7, Sc, Zr, Ti, and Si exhibit higher affinity with Fe and Ni. However, Sc and Zr are expensive. Conversely, Ti and Si [50] demonstrate an optimal balance between cost and impurity affinity for Fe and Ni.

To assess the capacity of the filter materials for chemically adsorbing gaseous impurities, we performed equilibrium thermodynamic calculations using FactSage based on the principle of Gibbs free energy minimization. The simulation was conducted at the filtration temperature of 793 K, with initial vapor-phase concentrations of Fe and Ni set to 10 ppm and 5 ppm. These values correspond approximately to the solid solubility of Fe and the critical corrosion tolerance limit of Ni in magnesium, respectively. When only Ti is present, the vapor-phase concentrations of Fe and Ni drop to about 8.05×10^{-6} and 3.56×10^{-8} ppm, respectively, indicating that Ti reacts with Fe and Ni atoms to form stable compounds and thus effectively removes them from the vapor phase. When both Ti and Si are used together, the gas concentrations of Fe and Ni are further reduced, demonstrating the superior adsorption capability of the Ti+Si composite filter for gaseous Fe and Ni atoms.

In summary, we designed a composite purification system: 1) using temperature gradients to let gaseous Mg and impurities atoms condense separately in different temperature zones, 2) using Ti and Si filter materials to adsorb gaseous impurity atoms that evaporate together with Mg, and 3) using Ti and Si filter materials to intercept solid-state Fe and Ni containing particles physically, which is expected to enable deep purification of electrolytic magnesium.

Table 2
Screening criteria of candidate filter materials for removing Fe and Ni impurities.

Category	Si	Mn	Ti	Cr	Cu	Zr	W	Co	Sc
Melting point (K)	1683	1517	1941	2180	1358	2128	3695	1768	1814
Formation energy eV/atom (Mg-X)	−0.11	0.02	0.07	0.011	−0.12	0.01	0.15	0.02	−0.03
Formation energy eV/atom (Fe-X)	−0.48	0.04	−0.42	0.03	0.06	−0.28	−0.02	−0.06	−0.27
Formation energy eV/atom (Ni-X)	−0.52	−0.36	−0.48	0.008	0.04	−0.46	−0.05	−0.02	−0.52
Price (CNY/kg)	10	14	50	65	80	167	216	247	26,500

Table 3
Impurity content (ICP-MS) in raw electrolytic magnesium and purified crystalline magnesium (ppm).

Category	Mg	Fe	Ni	Al	Si	Mn	Cu	Zn	Ti	Sn	Pb
Raw Mg	99.9%	258	12.6	23.9	24.3	14.1	6.9	15.5	<1	<1	1.1
Exp.1	99.98%	76	6	5	<20	6	1	1	<1	<1	<1
Exp.2	99.99%	28	1	4	<20	1	<1	2	<1	<1	<1
Exp.3	99.995%	4	<1	2	<20	<1	<1	<1	<1	<1	<1
Mg99.95B	99.95%	50	10	150	150	150	20	100	/	50	50
Mg99.99	99.99%	20	3	20	20	20	3	30	5	10	10

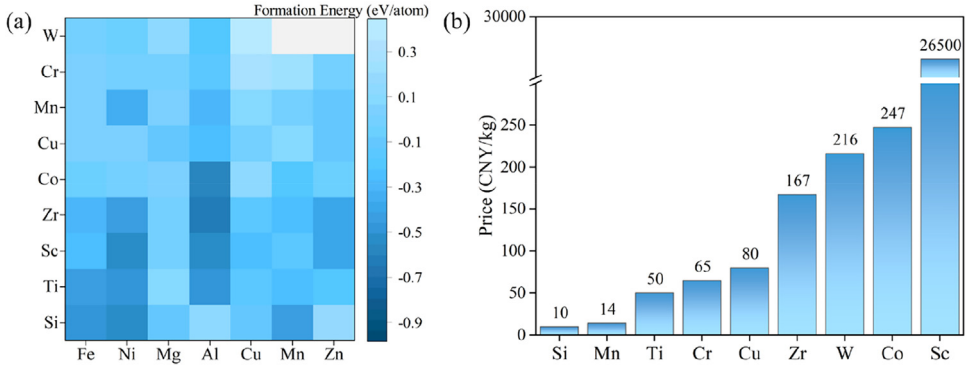


Fig. 7. Evaluation criteria for filter material selection. (a) Formation energies of intermetallic compounds with different elements (Gray cells denote missing data) [51–54]. (b) Market prices of candidate materials [55].

3.4. Purification experiment

To test the proposed purification strategies, we conducted three experiments: 1) vacuum sublimation, 2) sublimation with Ti mesh, and 3) sublimation with Ti mesh packed with Si particles. The experimental setups are shown in Fig. 8. In all cases, the raw Mg was placed at the furnace's bottom section, which was heated to 1073 K. The Ti mesh for experiment 2 and the Ti mesh with Si particles for experiment 3 were placed in the middle section at 973 K. Mg vapor was then condensed in a crystallizer located in the upper region, at a low temperature of 873 K. All experiments were conducted for 180 min.

The initial purity of the raw electrolytic Mg was 99.9%, with Fe and Ni content of 258 ppm and 12.6 ppm, respectively. The impurity levels in magnesium after vacuum sublimation are shown in Table 3 and Fig. 9. For experiment 1, the raw Mg was 112.4 g. After sublimation, 106.2 g of condensed Mg was collected, with 4.2 g residue remaining in the heating zone, the yield of high-purity magnesium was 98.2%. The purity of the collected Mg increased to 99.98%, with the Fe content dropping from 258 ppm to 76 ppm, and the Ni content reducing from 12.6 ppm to 6 ppm. Both Ni and other impurities fell below the 3N5B Mg standard, confirming effective removal of atoms. However, Fe content still exceeded the 3N5B standard (50 ppm). While the total purity reached 99.98%, Fe content remained above the 3N5B threshold (but within the 3N standard, 400 ppm), so the purified Mg was still classified as 3N. This suggests that sublimation alone is not enough for the deep removal of Fe, as many Fe impurities exist as particles, which can be carried by the Mg vapor flow and co-condense with Mg atoms, as previously analyzed. This underscores the need for filter materials to intercept these particles.

For experiment 2, Ti mesh filtration was employed to enhance impurity removal. 101.2 g of raw magnesium yielded 99.9 g of condensed magnesium, with a final yield of 98.7%. After the experiment, the Ti mesh changed color from bright white to dark yellow, with significant impurity deposits observed (Fig. 10a, b). Flocculent MgO inclusions were cap-

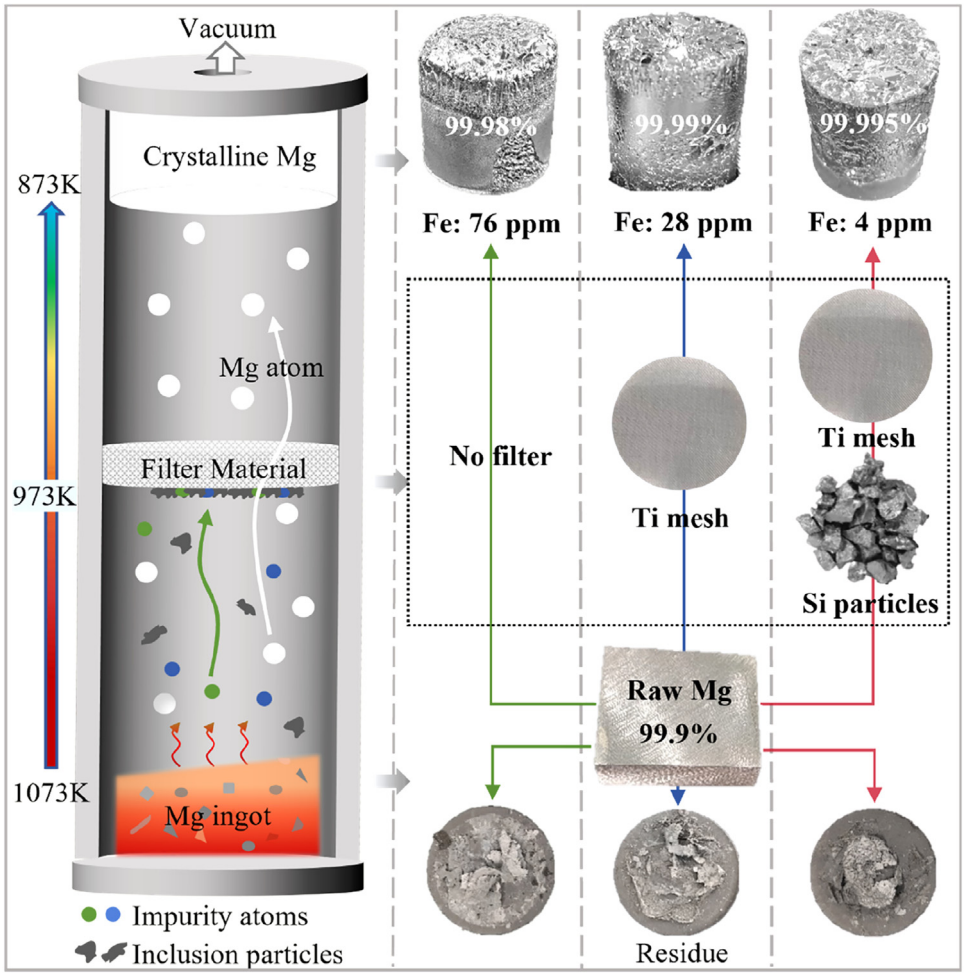


Fig. 8. The schematic diagram of the experimental apparatus.

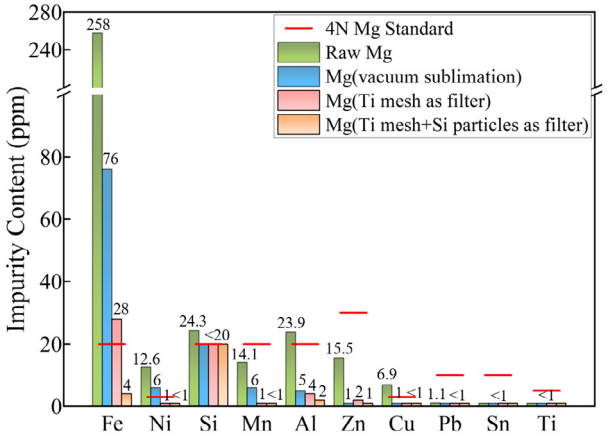


Fig. 9. Purification efficacy of vacuum sublimation coupled with filtration on key impurities in magnesium.

tured, and Fe-rich impurity particles accumulated on the mesh surface, as shown in Fig. 10c, d. This filtration reduced the Fe content to 28 ppm and the Ni content to 1 ppm, bringing the Ni level below the tolerance threshold of 5 ppm [26]. However, the Fe content remained above the 4N Mg standard (20 ppm), meaning the purified Mg, though reaching 4N total purity, could not be classified as 4N due to residual Fe.

To further enhance interception efficiency, experiment 3 introduced high-purity Si particles into the Ti mesh. The Si particles not only act as condensation sites for Fe atoms, but also enhance particle interception due to their three-dimensional stacked structure. For experiment 3, the raw Mg was 103 g and condensed Mg was 98.2 g, corresponding to a yield of 95.3%. The initially bright Si particles became dark, concurrent with the formation of a deposited layer on their surfaces (Fig. 11a, b). Due to the relatively dispersed distribution of impurities intercepted on the silicon particle surfaces, Fe-rich impurity particles and MgO were locally observed, as shown in Fig. 11c, d. The deposited layer contained Si, O, and Mg. Based on the characterization of structures and composition of the Si particles, we proposed two possible mechanisms for the formation of MgO layer. One involves the direct reaction of magnesium vapor with residual oxygen present in the vacuum system, leading to the deposition of MgO on the silicon particle surfaces. The other involves the decomposition and oxidation of Mg_2Si. As the local Mg vapor pressure increased, Mg reacted with Si to form Mg_2Si. As the Mg vapor pressure decreased at the end of sublimation, Mg_2Si decomposed and

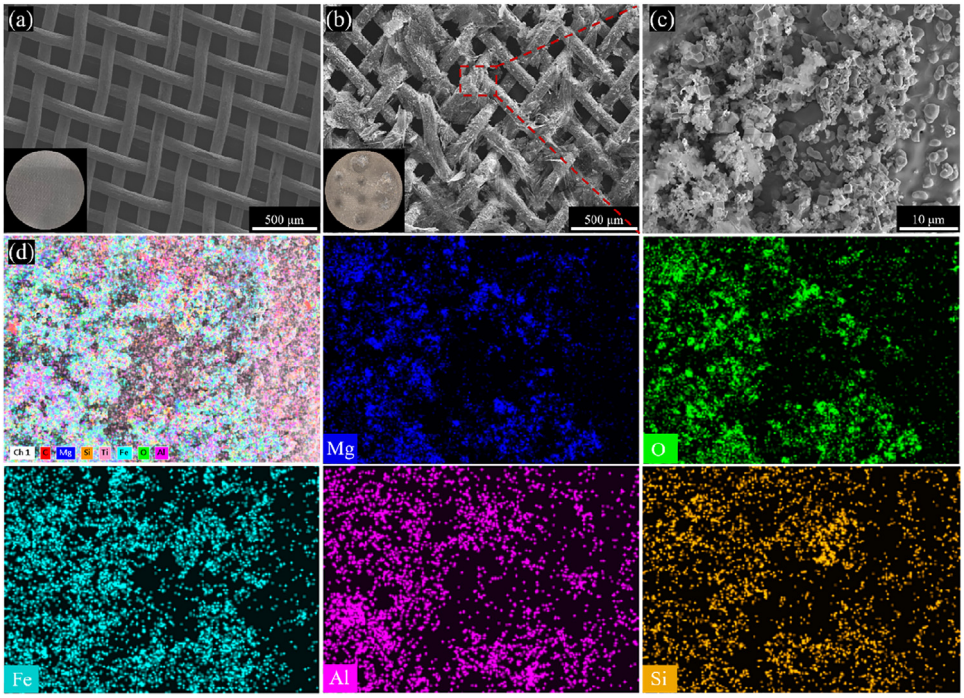


Fig. 10. Morphological and compositional characterization of titanium mesh before and after capturing impurities. (a) SEM image of titanium mesh before experiment. (b) SEM image of titanium mesh after experiment. (c) SEM image of the impurity particles in the selected area. (d) EDS mapping analysis of the captured impurity particles.

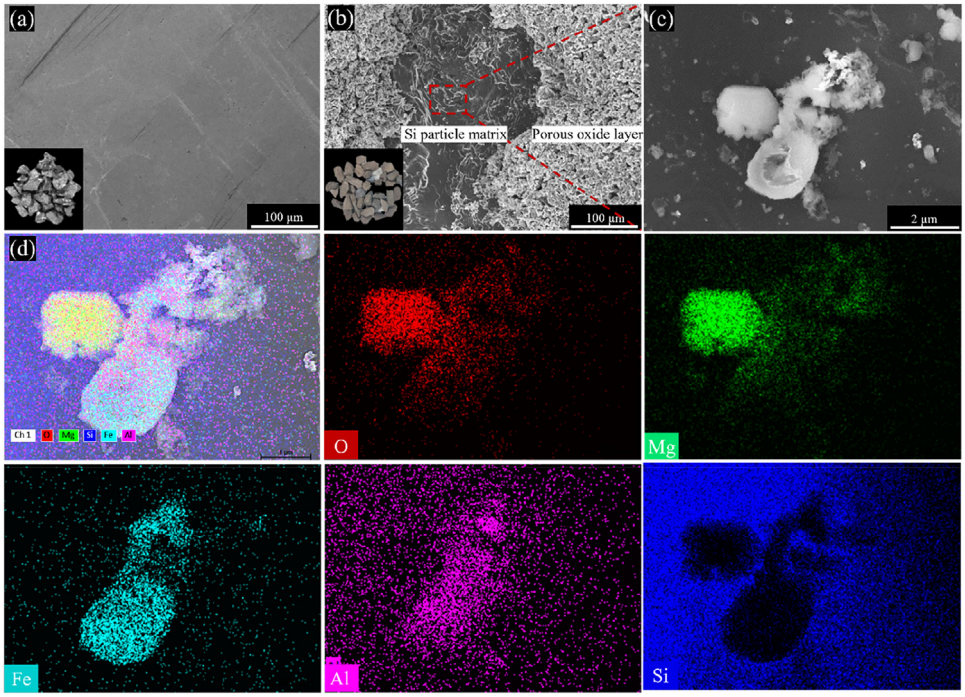


Fig. 11. Morphological and compositional characterization of silicon particles before and after capturing impurities. (a) SEM image of silicon particles before experiment. (b) SEM image of silicon particles after experiment. (c) SEM image of the impurity particles in the selected area. (d) EDS mapping analysis of the captured impurity particles.

released Mg vapor, leaving behind porous silicon. This process was also accompanied by the trace oxidation of Mg_2Si, which reacted with residual oxygen in the system to form MgO [56,57]. For the latter case, since these porous structures formed in the later stage of sublimation, they contribute little to impurity capture during the current experiment. However, if the silicon particles were reused, these porous structures could contribute to filtration. The use of this composite Ti-Si filter reduced the Fe content to 4 ppm, a level well below both the 4N Mg standard (20 ppm) and the solid solubility limit of Fe in Mg (10 ppm). Importantly, the introduction of Ti and Si filter materials did not lead to any detectable increase in Ti or Si content, confirming the absence of secondary contamination. After filtration, all measured impurities (Fe, Ni, Al, Ti, Si, Cu, Zn) complied with the 4N Mg standard (GB/T 3499-2023), yielding magnesium with 99.995% purity.

3.5. Corrosion experiment

We evaluated the purification effect through immersion corrosion testing in 3.5% NaCl solution at room temperature. Samples of raw electrolytic magnesium (99.9%) and purified magnesium (99.995% from experiment 3) were cut into 15 mm × 15 mm × 5 mm pieces. After one day of immersion, the raw magnesium displayed severe localized corrosion, while the purified magnesium, after six days of immersion, exhibited only minor pitting with isolated pits.

To quantify the corrosion rates, we measured hydrogen gas evolution. The hydrogen evolution corrosion rate (mm/y) was calculated using the following equation [58]:

$$P_H = 2.279\frac{H_i - H_f}{At}$$

where P_H is the hydrogen evolution corrosion rate (mm/y), H_i and H_f are the initial and final numerical values of the burette (mL), respectively, A is the sample surface area (cm^2), and t is the immersion time (d).

The hydrogen evolution corrosion rates for raw magnesium and purified magnesium were 284.58 mm/y and 0.14 mm/y, respectively. The severe corrosion in raw magnesium is driven by Fe-rich impurities, particularly Fe-bearing intermetallic compounds. Their notably higher electrode potential compared to elemental Fe established them as highly efficient cathodic sites, drastically accelerating galvanic corrosion of the Mg matrix [21]. The corrosion rate of purified magnesium represents a three–order–of–magnitude reduction from the raw material, aligning with the range reported for high–purity magnesium (<1 mm/y) [59,60]. These results demonstrate that targeted removal of particulate impurities via integrated sublimation and filtration is essential for attaining both higher purity and superior corrosion performance in electrolytic magnesium.

4. Conclusion

This study establishes an impurity-speciation strategy to upgrade electrolytic magnesium by combining vapor-phase separation with targeted interception of impurity-bearing particulates. By linking the physical/chemical forms of Fe to its transport behavior during sublimation, we identified why sublimation alone is less effective in removing Fe impurities and then demonstrated an integrated route to deep purification.

(1) Impurity speciation in electrolytic Mg. In electrolytic magnesium, Fe is present mainly as Fe-bearing inclusions, dominated by elemental Fe particles, with smaller fractions as solid-solution Fe and intermetallic compounds (e.g., Al_3FeSi_2 and $Fe_{0.42}Si_{2.67}$). The inclusions are predominantly micrometer-scale, with an average size of approximately 2.3 μm.
(2) Mechanism limiting sublimation-only purification. Force-balance analysis indicates that inclusions of the types and sizes observed here can be entrained by magnesium vapor during vacuum sublimation and subsequently co-deposited during crystallization. This particulate carry-over, rather than the volatility of dissolved Fe alone, is the primary barrier to deep Fe removal and motivates the need for in-line interception.
(3) Rational design of the in-line trap. Based on thermal stability, selective interaction with Fe and Ni species, and cost, Ti mesh packed with Si particles was selected as the filter media. The trap provides both physical interception of entrained inclusions and additional capture of impurity species in the vapor stream.

Overall, these results demonstrate that controlling particulate transport is essential for deep purification of electrolytic magnesium and provide a practical framework for designing purification routes that start from impurity form, not only equilibrium volatility.

Declaration of competing interest

Zhiwei Shan is an editorial board member/editor-in-chief for Journal of Magnesium and Alloys and was not involved in the editorial review or the decision to publish this article. All authors declare that there are no competing interests.

CRediT authorship contribution statement

Bingbing Gao: Writing – original draft, Methodology, Investigation, Formal analysis, Data curation. **Bo Yang:** Writing – review & editing, Methodology, Investigation. **Rui Zheng:** Writing – review & editing, Methodology, Investigation. **Boyu Liu:** Writing – review & editing, Writing – original draft, Supervision, Methodology, Funding acquisition. **An Wang:** Investigation, Formal analysis. **Jiuzhang Li:** Investigation, Formal analysis. **Hangwei Cui:** Investigation, Formal analysis. **Zhiwei Shan:** Writing – review & editing, Supervision, Funding acquisition, Conceptualization.

Acknowledgments

The authors gratefully acknowledge the support of the National Natural Science Foundation of China (52371121,

U24A2021 and 523B2001), the National Key Research and Development Program of China (No. 2022YFB3709300), the Innovation Capability Support Program of Shaanxi (Program No. 2023ZSJD-05), and Xi'an Key Laboratory for Light Alloys (201805064ZD15CG48). We thank Jia-Yu Cai, Lei Cai, and Xiaohua Cheng from Xi'an Jiaotong University for their assistance with the purification experiments, corrosion experiments and result analyses, respectively.

Supplementary materials

Supplementary material associated with this article can be found, in the online version, at doi:10.1016/j.jma.2026.102109.

References

[1] Y. Yang, X.M. Xiong, J. Chen, X.D. Peng, D.L. Chen, F.S. Pan, J. Magnes. Alloys 9 (3) (2021) 705–747, doi:10.1016/j.jma.2021.04.001.
[2] J.F. Song, J. She, D.L. Chen, F.S. Pan, J. Magnes. Alloys 8 (1) (2020) 1–41, doi:10.1016/j.jma.2020.02.003.
[3] D. Bernhardt, J.F. Reilly, Mineral commodity summaries 2021[R], U.S. Geological Survey, Reston, VA, 2021.
[4] Y. Yuan, X. Chen, X. Xiong, K. Li, J. Tan, Y. Yang, X. Peng, X. Chen, D. Chen, F. Pan, J. Magnes. Alloys 13 (2025) 4689–4732.
[5] Y. Yang, X. Xiong, J. Chen, X. Chen, X. Peng, F. Pan, J. Magnes. Alloys 13 (2025) 1855–1858.
[6] J. She, J. Chen, X. Xiong, Y. Yang, X. Peng, D. Chen, F. Pan, J. Magnes. Alloys 12 (2024) 3441–3475.
[7] W. Wang, S.Y. Yan, Light Met. 10 (2022) 47–51, doi:10.13662/j.cnki.qjs.2022.10.011.
[8] T. Ma, B. Yang, Y. Tian, N. Xiong, B. Xu, G. Zha, R. Yu, D. Liang, L. Wang, D. Wang, J. Magnes. Alloys 13 (2025) 731–745.
[9] C. Sim, H.-J. Jeoung, J. Kang, J. Magnes. Alloys 13 (2025) 5538–5548.
[10] Y.S. Che, Y.Z. Li, J.X. Song, J.L. He, World Nonferrous Met. 580 (16) (2021) 5–9, doi:10.3969/j.issn.1002-5065.2021.16.002.
[11] Z.W. Shan, Y.C. Wang, P.F. Wang, Y.Z. Ma, R. Zheng, Mater. China 43 (1) (2024) 46–53, doi:10.7502/j.issn.1674-3962.202302004.
[12] Y.F. Liu, Y. Zhang, W.J. Yu, X. Liu, Resour. Sci. 37 (5) (2015) 1047–1058 CNKI:SUN:ZRZY.0.2015-05-022.
[13] P. Duhaime, P. Mercille, M. Pineau, Miner. Process. Extr. Metall. 111 (2) (2002) 53–55, doi:10.1179/mpm.2002.111.2.53.
[14] F.X. Zhu, L. Li, K.H. Li, Z. Sheng, K.H. Qiu, Light Met. 11 (2019) 45–50, doi:10.13662/j.cnki.qjs.2019.11.011.
[15] Y.J. Zhang, Magnesium Electrolysis Production Technology[M], Central South University Press, Changsha, 2006.
[16] J.D. Hanawalt, C.E. Nelson, J.A. Peloubet, Trans. Am. Inst. Min. Metall. Pet. Eng. 147 (1942) 273–299.
[17] M. Liu, P.J. Uggowitzer, A.V. Nagasekhar, P. Schmutz, M. Easton, G.L. Song, A. Atrens, Corros. Sci. 51 (3) (2009) 602–619, doi:10.1016/j.corsci.2008.12.015.
[18] Z. Qiao, Z. Shi, N. Hort, N.I.Z. Abidin, A. Atrens, Corros. Sci. 61 (2012) 185–207, doi:10.1016/j.corsci.2012.04.030.
[19] N. Birbilis, G. Williams, K. Gusieva, A. Samaniego, M.A. Gibson, H.N. Mcmurray, Electrochem. Commun. 34 (2013) 295–298, doi:10.1016/j.elecom.2013.07.021.
[20] A.D. King, N. Birbilis, J.R. Scully, Electrochim. Acta 121 (2014) 394–406, doi:10.1016/j.electacta.2013.12.124.
[21] L. Yang, G.K. Liu, L.G. Ma, E.L. Zhang, X.R. Zhou, G. Thompson, Corros. Sci. 139 (2018) 421–429, doi:10.1016/j.corsci.2018.04.024.
[22] G.L. Makar, J. Kruger, Int. Mater. Rev. 38 (3) (1993) 138–153, doi:10.1179/imr.1993.38.3.138.
[23] B. Yang, B.Y. Liu, H. Yang, Z.W. Shan, Mater. China 39 (7) (2020) 576–584, doi:10.7502/j.issn.1674-3962.202006033.
[24] H.X. Cao, M.T. Huang, C.C. Wang, S.Y. Long, J.L. Zha, G.Q. You, J. Magnes. Alloys 7 (3) (2019) 370–380, doi:10.1016/j.jma.2019.07.002.
[25] R. Yu, Y. Tian, B. Yang, B.Q. Xu, D. Liang, L.P. Wang, Chin. J. Nonferrous Met. 34 (1) (2024) 229–253, doi:10.11817/j.ysxb.1004.0609.2023-44147.
[26] S.C. Zhen, G.D. Li, China Met. Bull. 12 (2019) 95–97, doi:10.3969/j.issn.1672-1667.2019.12.058.
[27] J.I. Kim, H.N. Nguyen, B.S. You, Y.M. Kim, Scr. Mater. 162 (2019) 355–360, doi:10.1016/j.scriptamat.2018.11.046.
[28] T. Chen, Y. Yuan, T.T. Liu, D.J. Li, A.T. Tang, X.H. Chen, S.F. Rainer, F.S. Pan, JOM 73 (3) (2021) 892–902, doi:10.1007/S11837-020-04550-5.
[29] G.H. Wu, H.H. Zou, C.Q. Zhai, K. Zeng, W.J. Ding, Foundry 52 (3) (2003) 167–170.
[30] G.H. Wu, H.T. Gao, W.J. Ding, Y.P. Zhu, J. Mater. Sci. 40 (23) (2005) 6175–6180, doi:10.1007/s10853-005-3161-7.
[31] J. Wang, Y. Yuan, Y. Zhang, X.H. Feng, T. Chen, X.H. Chen, B. Jiang, Y.S. Yang, F.S. Pan, Vacuum 203 (2022) 111310, doi:10.1016/J.VACUUM.2022.111310.
[32] X.L. Li, T.G. Zhang, Y. Liu, J.H. Guo, J.Z. Xu, Y.Y. Liang, J. Magnes. Alloys 13 (2025) 3134–3149.
[33] D. Wang, T.A. Zhang, J.Z. Xu, K. Wang, J. Magnes. Alloys 13 (2025) 2470–2499.
[34] D. Liang, L.P. Wang, Y. Tian, B. Yang, B.Q. Xu, W. Zhao, T.Z. Ma, Sep. Purif. Technol. 327 (2023) 124878, doi:10.1016/J.SEPPUR.2023.124878.
[35] G.Z. Zha, Y.K. Wang, M.Q. Cheng, D.X. Huang, W.L. Jiang, B.Q. Xu, B. Yang, J. Mater. Res. Technol. 9 (3) (2020) 2926–2933, doi:10.1016/j.jmrt.2020.01.043.
[36] Y.C. Wang, T. Yang, T. Qu, B. Yang, Y.N. Dai, Y.P. Sun, Mater. Sci. Forum. 788 (2014) 52–57, doi:10.4028/www.scientific.net/MSF.788.52.
[37] S.R. Mohamed, S. Friedrich, B. Friedrich, Metals (Basel) 9 (1) (2019) 85, doi:10.3390/met9010085.
[38] Z.S. Ma, S.R. Ma, F.X. Zhu, K.H. Li, Z. Sheng, Z.J. Li, Y.W. Wang, Metals (Basel) 13 (4) (2023) 811, doi:10.3390/met13040811.
[39] D. Liang, L. Wang, T. Ma, R. Yu, Y. Tian, B. Xu, B. Yang, J. Magnes. Alloys 13 (2025) 2813–2824.
[40] Q. Li, Z.F. Hu, Z.Q. Li, H.L. Jiang, Y.X. Yin, J.T. Jia, Nonferrous Met. 4 (6) (2014) 21–23, doi:10.3969/j.issn.2095-1744.2014.06.007.
[41] G. Revel, J.L. Pastol, J.C. Rouchaud, R. Fromageau, Metall. Trans. B 9 (4) (1978) 665–672, doi:10.1007/BF03257216.
[42] R. Zheng, B. Yang, A. Wang, B.Y. Liu, P.F. Wang, Z.W. Shan, Chin. J. Nonferrous Met. 33 (07) (2023) 2347–2355, doi:10.11817/j.ysxb.1004.0609.2022-43717.
[43] F.X. Zhu, L. Li, K.H. Li, Z. Sheng, K.H. Qiu, Light Met. 11 (2019) 45–50.
[44] Y.N. Dai, B. Yang, Non-ferrous Metal Vacuum Metallurgy, 2nd ed., Metallurgical Industry Press, Beijing, 2009.
[45] X.F. Kong, B. Yang, H. Xiong, D.C. Liu, B.Q. Xu, Vacuum 105 (2014) 17–20, doi:10.1016/j.vacuum.2014.01.012.
[46] C.Y. Dong, W.L. Luan, S.T. Zhou, Q. Zhang, J. China Univ. Pet. (Ed. Nat. Sci.) 31 (5) (2007) 55–59 63, doi:10.3321/j.issn:1000-5870.2007.05.012.
[47] M. Chen, S.J. Zhang, R.B. Li, J.J. Nan, J.H. Liu, P.X. Yang, J. Zhengzhou Univ.(Eng. Sci. 44 (4) (2023) 88–93, doi:10.13705/j.issn.1671-6833.2023.01.014.
[48] N. Singh, M. Kroells, C. Li, E. Ching, M. Ihme, C.J. Hogan, T.E. Schwartzentruber, AIAA J. 60 (2) (2022) 587–597, doi:10.2514/1.J060648.
[49] S.Q. Huang, Y.R. Nie, X.J. Shen, Course in Thermodynamics, 2nd ed., Beijing, 1994.
[50] Z.W. Shan, B. Yang, P.F. Wang, B.Y. Liu, Application of elemental silicon filter material in gas-phase magnesium purification and production system containing the same[P], 2021 China Patent CN110724833B.
[51] A. Jain, S.P. Ong, G. Hautier, W. Chen, W.D. Richards, S. Dacek, S. Cholia, D. Gunter, D. Skinner, G. Ceder, K.A. Persson, APL Mater. 2013, 1(1), 011002. doi:10.1063/1.4812323.

[52] Materials project (2011). https://materialsproject.org (accessed 5 January 2026).
[53] M. de Jong, W. Chen, T. Angsten, Jain A., Notestine R., Gamst A., Sluiter M., Krishna Ande C., van der Zwaag S., Plata J.J., Toher C., Curtarolo S., Ceder G., Persson K.A., Asta M. Sci. Data 2: 150009 (2015). doi:10.1038/sdata.2015.9.
[54] M. de Jong, W. Chen, H. Geerlings, M. Asta, K.A. Persson Sci. Data 2: 150053 (2014). doi:10.1038/sdata.2015.53.
[55] CBC IE, 2014. https://www.cbcie.com/ (accessed 5 January 2026).
[56] S.M. Hwang, S.J. Park, G.T. Kim, H.N. Kim, J.W. Ko, Y.H. Park, D.W. Lee, Mater. Trans. 62 (2021) 1285–1290, doi:10.2320/matertrans.MT-M2020396.
[57] J. Tani, M. Takahashi, H. Kido, 18, 2011, 142013, doi:10.1088/1757-899X/18/14/142013.
[58] B. Jiang, Q. Xiang, A. Atrens, J.F. Song, F.S. Pan, Corros. Sci. 126 (2017) 374–380, doi:10.1016/j.corsci.2017.08.004.
[59] S.K. Woo, Suh B.C, H.S. Kim, C.D. Yim, Corros. Sci. 184 (2021) 109357, doi:10.1016/j.corsci.2021.109357.
[60] F.Y. Cao, Z.M. Shi, J. Hofstetter, P.J. Uggowitzer, G.L. Song, M. L, A. Atrens, Corros. Sci. 75 (OCT) (2013) 78–99, doi:10.1016/j.corsci.2013.05.018.